Geophysical Research Letters

RESEARCH LETTER
10.1029/2024GL110728

Air-Sea Heat and Moisture Flux Gradients

Rhys Parfitt[1]

[1]Department of Earth, Ocean, and Atmospheric Science, Florida State University, Tallahassee, FL, USA

Key Points:

- Air-sea heat and moisture flux gradients modulate important oceanic and atmospheric processes across a multitude of spatiotemporal scales
- Air-sea heat flux gradient variability can statistically precede mid-latitude atmospheric variability
- Notable air-sea heat and moisture flux gradient inconsistencies exist in data products, yet the ability to validate them remains elusive

Supporting Information:

Supporting Information may be found in the online version of this article.

Correspondence to:

R. Parfitt,
rparfitt@fsu.edu

Citation:

Parfitt, R. (2024). Air-sea heat and moisture flux gradients. *Geophysical Research Letters*, *51*, e2024GL110728. https://doi.org/10.1029/2024GL110728

Received 9 JUN 2024
Accepted 4 NOV 2024

Abstract Air-sea heat and moisture fluxes modulate the surface energy balance and oceanic and atmospheric heat transport across all timescales. Spatial gradients of these fluxes, on a multitude of spatial scales, also have significant impacts on the ocean and atmosphere. Nevertheless, analysis of these gradients, and discussion regarding our ability to represent them, is relatively absent within the community. This letter discusses their importance and presents a wintertime climatology. Their sensitivity to spatiotemporal scale and choice of data set is also examined in the mid-latitudes. A lead-lag analysis illustrates that wintertime air-sea heat flux gradients in the Gulf Stream can precede the North Atlantic Oscillation by ∼1 month. A lack of observations and thus validation of air-sea heat flux gradients represents a significant gap in our understanding of how air-sea processes affect weather and climate, and warrants increased attention from the observational and modeling communities.

Plain Language Summary The oceans impact both weather and climate by heating and cooling the lower atmosphere. Surface latent (sensible) heat flux is a quantity that measures the exchange of heat associated with evaporation of seawater (an air-sea temperature difference). In addition to the absolute exchange, the manner in which the exchange varies spatially (the heat flux gradients) is also known to be important for the development of weather systems and longer-term climate. Despite this, relatively little attention is paid in the literature to variability in these gradients. This study provides a brief overview of their importance and provides a wintertime climatology in these gradients. It is also illustrated that when considering gradients, the importance of specifying the spatial scale over which the gradient is calculated is critical. Although many differences exist between air-sea heat flux data products in these gradients, there are currently almost no observations to validate them in key areas of interest, which represents a significant deficiency in our understanding of ocean-atmosphere interactions. This is emphasized by demonstrating that these gradients in the mid-latitudes can statistically precede variability in the North Atlantic Oscillation, the most important mode of monthly atmospheric variability in the North Atlantic.

1. Introduction

The ocean dominates the zonally integrated poleward heat transport from the tropics into the sub-tropics and mid-latitudes (Trenberth & Caron, 2001), where it transfers vast amounts of heat and moisture into the atmosphere via latent and sensible heat fluxes (LHFs and SHFs respectively). These fluxes are estimated through air-sea differences in the mean "bulk" state variables measured at the surface and at some height within the surface layer (Cronin et al., 2019):

$$\mathrm{LHF} \approx \rho L_v C_E S \Delta Q,$$

$$\mathrm{SHF} \approx \rho c_p C_H S \Delta \theta,$$

where ρ is density of air, S is scalar wind speed relative to the ocean surface (including gustiness), C_E and C_H are drag coefficients for latent and sensible heat respectively, L_v is latent heat of evaporation, c_p is specific heat at constant pressure, and ΔQ and $\Delta\theta$ are air-sea differences in specific humidity and potential temperature respectively.

These heat fluxes are well-documented in their impact on the atmosphere and ocean, particularly in the wintertime extra-tropics when LHFs and SHFs are generally much larger due primarily to increased ΔQ and $\Delta\theta$ (e.g., Yu & Weller, 2007). This is particularly true over western boundary currents (WBCs) in the Northern Hemisphere (NH), where climatological maxima are located due to frequent cold and dry air blowing off large land masses over warm waters. Here, strong air-sea exchange significantly modulates storm-development (Cione et al., 1993;

Hirata et al., 2019), and anchors vertical motion deep into the troposphere (Minobe et al., 2008). Generally, air-sea heat fluxes exhibit some of the highest uncertainties of earth system variables in observations and models (e.g., Robertson et al., 2020), and significant efforts are being made to improve their accuracy.

These regions are also characterized by frequent extremely large air-sea flux gradients (e.g., Parfitt et al., 2016). Such gradients also have an important role in modulating atmospheric and oceanic variability. The exact role likely depends on the spatial scale associated with the gradient. For example, "oceanic baroclinic adjustment" (Hotta & Nakamura, 2011; Nakamura et al., 2004; Taguchi et al., 2009), suggested as a critical component in maintaining baroclinicity in the mid-latitude storm-tracks of both the Northern and Southern Hemisphere (SH), is primarily associated with a large-scale air-sea heat flux gradient (>100 km). Here, a strong surface air-temperature gradient formed through differential sensible heat fluxes above an oceanic front favors baroclinic eddy growth (c.f. Figure 12, Sampe et al., 2010). Air-sea heat flux gradients are also known to impact frontogenesis in the lower atmosphere (Jacobs et al., 2008; Reeder et al., 2021; Tochimoto & Niino, 2022), thus modulating the extra-tropical transition of tropical cyclones (Jones et al., 2023) and time-mean structures (Jones et al., 2024; Parfitt & Seo, 2018), with studies indicating fine-scale gradients (∼25 km) are critical (Parfitt et al., 2016). Furthermore, this effect can overcome data assimilation constraints in reanalysis data sets (Masunaga et al., 2018; Parfitt, Czaja, & Kwon, 2017). Differential air-sea heat fluxes also modulate oceanic frontogenesis in oceanic frontal regions (Tozuka & Cronin, 2014; Tozuka et al., 2017), with implications for the aforementioned mechanisms, coupled air-sea feedbacks and climate model evaluation.

Despite the clear importance of air-sea heat flux gradients, they remain relatively undiscussed in the air-sea interaction and wider weather and climate communities. For example, there are no comprehensive data set comparisons in air-sea heat flux gradients, despite many in air-sea heat fluxes. To the author's knowledge, a published climatology also does not exist. Furthermore, other than rare instances (e.g., Kawai et al., 2015), in virtually all open ocean regions of interest there is no in situ data to validate models and data products for air-sea heat flux gradients at the aforementioned scales. This is because one requires observations from multiple measurement systems located at a continually consistent distance close (<100 km) to each other. Buoys fitting this criterion are generally located very near the coast (see the National Data Buoy Center for example, https://www.ndbc.noaa.gov/), and individual ship-based measurements are not suitable for this purpose. Satellite-derived flux products are also not suitable given that input variables come from different satellites with different overpass times (Gentemann et al., 2020).

The data sets used in this study are introduced in Section 2. In Section 3, a wintertime air-sea heat flux gradient climatology is considered. A case study is also discussed in the context of atmospheric storms, with attention paid to the spatial scale over which the gradient is calculated. To demonstrate uncertainty, three products are used to conduct a comparison at a location in the Gulf Stream (GS). The relationship at this location of both SHF and the SHF gradient with atmospheric and oceanic variability is also explored. Section 4 presents conclusions and offers potential future directions.

2. Data

Air-sea heat fluxes from three products are used in this study. The first data set used is the European Center for Medium-Range Weather Forecasts Reanalysis 5 (ERA-5) product (Hersbach et al., 2020), from 1979 to 2018. ERA5 has a native resolution of ∼0.28° and is provided on a regular 0.25° grid. LHFs and SHFs are provided every hour, and represent an accumulation across the previous hour ending at the validity time. As such, a representative value of LHF (Wm^{-2}) at any particular hour t is estimated as $\left(\frac{1}{3600}\right)\left[\frac{1}{2}\left(\mathrm{LHF}_t\right) + \frac{1}{2}\left(\mathrm{LHF}_{t+1}\right)\right]$.

The second data set used is the Japanese 55-year Reanalysis (JRA-55) product (Kobayashi et al., 2015), from 1979 to 2018. JRA-55 has a native resolution of ∼0.50° and provides all variables on a regular 1.25° grid, which is used here (it is noted that many variables, including LHF and SHF, are also provided on a ∼0.50° grid). In JRA-55, two datapoints are provided every 6 hr, representing averages of 3-hr and 6-hr forecasts from that time. Accordingly, a representative value of LHF (Wm^{-2}) at a particular 6-hourly time t can be estimated from the formula $\frac{1}{2}\left[\left(2\mathrm{LHF}_{t-1}^{6-\mathrm{hour}} - \mathrm{LHF}_{t-1}^{3-\mathrm{hour}}\right) + \mathrm{LHF}_{t}^{3-\mathrm{hour}}\right]$.

Lastly, a blended product Woods Hole Oceanographic Institution Objectively Analyzed Air-Sea Fluxes Version 3 (OAFlux-v3) is used from 1985 to 2018. OAFlux-v3 uses an integrated analysis method to combine satellite and

reanalysis data, and the COARE 3.0 algorithm to calculate heat fluxes (Jin & Weller, 2008). OAFlux-v3 is provided as daily means on a regular 1° grid.

In addition to LHF and SHF, ERA-5 is also used for sea-surface temperature (SST), mean sea-level pressure (MSLP), as well as 900 hPa air-temperature (T_{900}), zonal wind and meridional wind. Atmospheric frontal systems are calculated from the equation $\frac{|\nabla T_{900}|\zeta_{900}}{f|\nabla T_o|}$, where ζ_{900} is 900 hPa relative vorticity, f is the Coriolis parameter, and $|\nabla T_o|$ is a typical temperature gradient 0.45 K/100 km, as in Parfitt, Czaja, and Seo (2017).

3. Results

3.1. Wintertime Climatology

Figure 1a illustrates the meridional SHF gradient climatology in wintertime (December-February, DJF, in the NH; June-August, JJA, in the SH). The gradient is calculated at each point in ERA-5 from the SHF values (hourly, but sampled 6-hourly) at each neighboring meridional grid point, and as such the scale of the gradient is ∼50 km. For the rest of the paper, this is written as $\left(\frac{d\text{SHF}}{dy}\right)_{\sim 50\text{km}}$, where the temporal resolution is 6-hourly calculated as described in Section 2 unless specified otherwise. Although the units of all LHF and SHF gradients in this manuscript are given in Wm^{-2}/100 km, the scale over which the gradient is calculated is important and will be specified. It is noted that the meridional SHF gradient is illustrated instead of the absolute gradient magnitude to retain the sign, which is important for the associated air-sea interaction processes (Parfitt et al., 2016). The meridional temperature gradient is also most relevant for baroclinity (Walland & Simmonds, 1999), and hence mid-latitude storm development in general. For reference, zonal gradients are shown in Figure S1 in Supporting Information S1.

In the NH, the largest average $\left(\frac{d\text{SHF}}{dy}\right)_{\sim 50\text{km}}$ magnitudes (∼50 Wm^{-2}/100 km) are typically in regions associated with large meridional SST gradients. In the North Atlantic, this is across the GS, the Labrador Current, and the Greenland Current. In the North Pacific, this is in the Sea of Japan, across the Kuroshio-Oyashio Current system, and in the north of the Bering Sea. This is also true in the SH, with large average $\left(\frac{d\text{SHF}}{dy}\right)_{\sim 50\text{km}}$ magnitudes found at the Agulhas Return Current and Brazil-Malvinas Confluence Region, as well as oceanic frontal zones along the Antarctic Circumpolar Current, although they are generally smaller than their NH counterparts. It is noted that the largest average $\left(\frac{d\text{SHF}}{dy}\right)_{\sim 50\text{km}}$ magnitudes, however, are comparable and are found near the sea-ice margin off the coast of Antarctica.

Figure 1b illustrates the analogous wintertime $\left(\frac{d\text{LHF}}{dy}\right)_{\sim 50\text{km}}$ climatology. There is a high degree of similarity in spatial structure with Figure 1a, with the largest average $\left(\frac{d\text{LHF}}{dy}\right)_{\sim 50\text{km}}$ corresponding to regions of high meridional SST gradients. Across the GS and Kuroshio-Oyashio systems however, the average magnitude is almost double that of $\left(\frac{d\text{SHF}}{dy}\right)_{\sim 50\text{km}}$, reaching ∼100 Wm^{-2}/100 km, while off the coast of Antarctica the average magnitude is greatly reduced. The presence of wintertime average $\left(\frac{d\text{LHF}}{dy}\right)_{\sim 50\text{km}}$ magnitudes up to ∼20 Wm^{-2}/100 km are also noted in the Tropics.

Recent studies suggest the ocean is the primary driver of co-variability between mid-latitude SSTs and air-sea heat and moisture fluxes at the oceanic mesoscale (Bishop et al., 2017; Small et al., 2019). It is thus not surprising that in the mid-latitudes, the structure of $\left(\frac{d\text{SHF}}{dy}\right)_{\sim 50\text{km}}$ and $\left(\frac{d\text{LHF}}{dy}\right)_{\sim 50\text{km}}$ variability closely mirrors that of meridional SST gradients. In general, climatological $\left(\frac{d\text{SHF}}{dy}\right)_{\sim 50\text{km}}$ and $\left(\frac{d\text{LHF}}{dy}\right)_{\sim 50\text{km}}$ act to enhance (reduce) the climatological meridional atmospheric temperature gradients in both the NH and SH on the poleward (equatorward) side of warm currents such as the mid-latitude frontal zones, suggesting variability in latitude of these zones will likely influence atmospheric variability (Joyce et al., 2019).

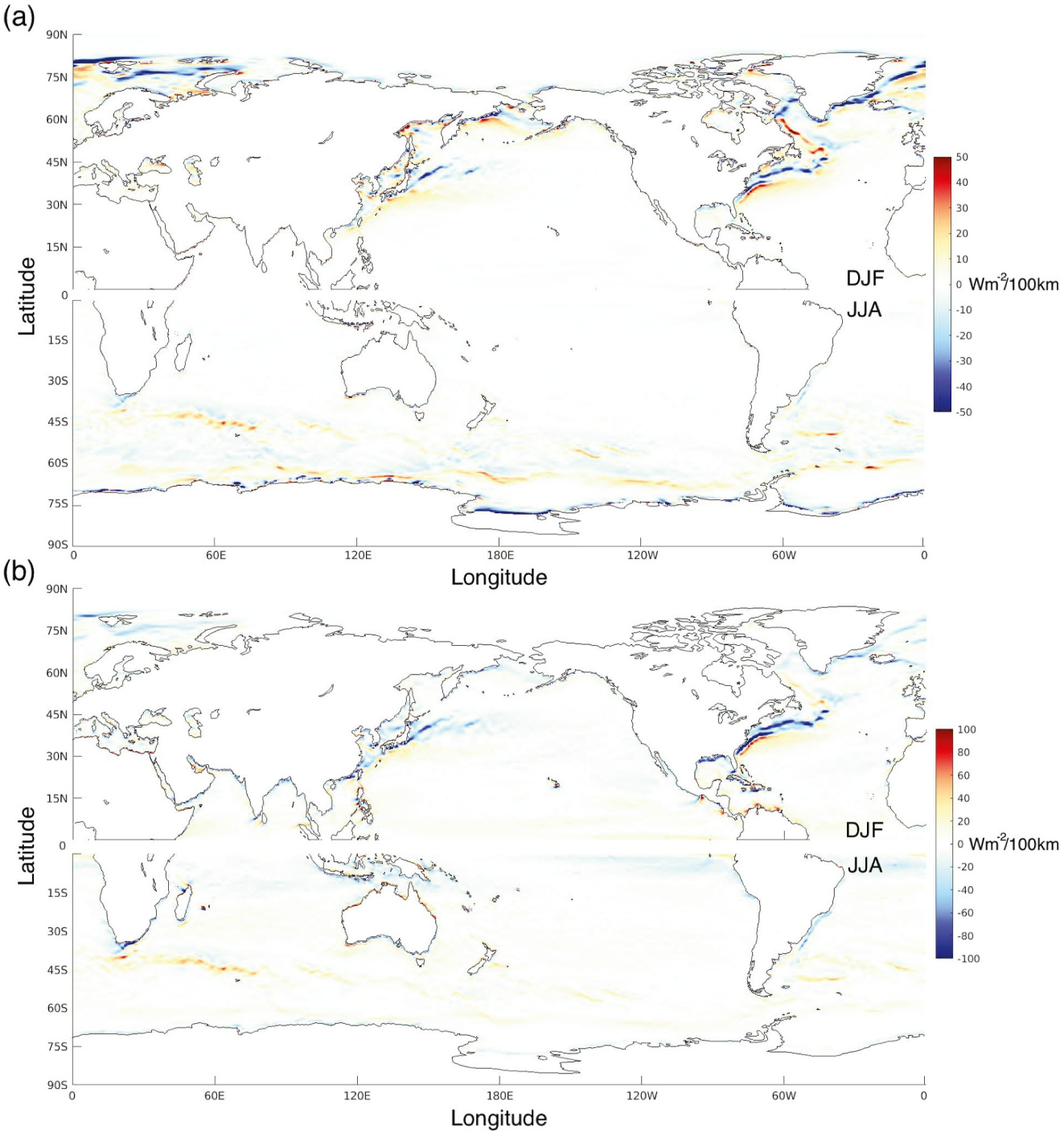

Figure 1. Wintertime (DJF in NH, JJA in SH, 1979–2018) climatology of (a) $\left(\frac{d\text{SHF}}{dy}\right)_{\sim 50\text{km}}$ and (b) $\left(\frac{d\text{LHF}}{dy}\right)_{\sim 50\text{km}}$ in ERA-5. Positive is defined as northward.

3.2. Case Study and Importance of Scale

As discussed in the introduction, LHF and SHF gradients in the "hotspot" regions in Figure 1, such as WBCs, can impact weather systems both through direct influence and pre-conditioning. The gradient spatial scale, however, is critically important to the interaction. Figure 2 considers a case study of an extra-tropical cyclone across the GS on 1200UTC 20 January 1979 in ERA-5. Figure 2a illustrates the MSLP (dotted contours) and atmospheric cold

10.1029/2024GL110728

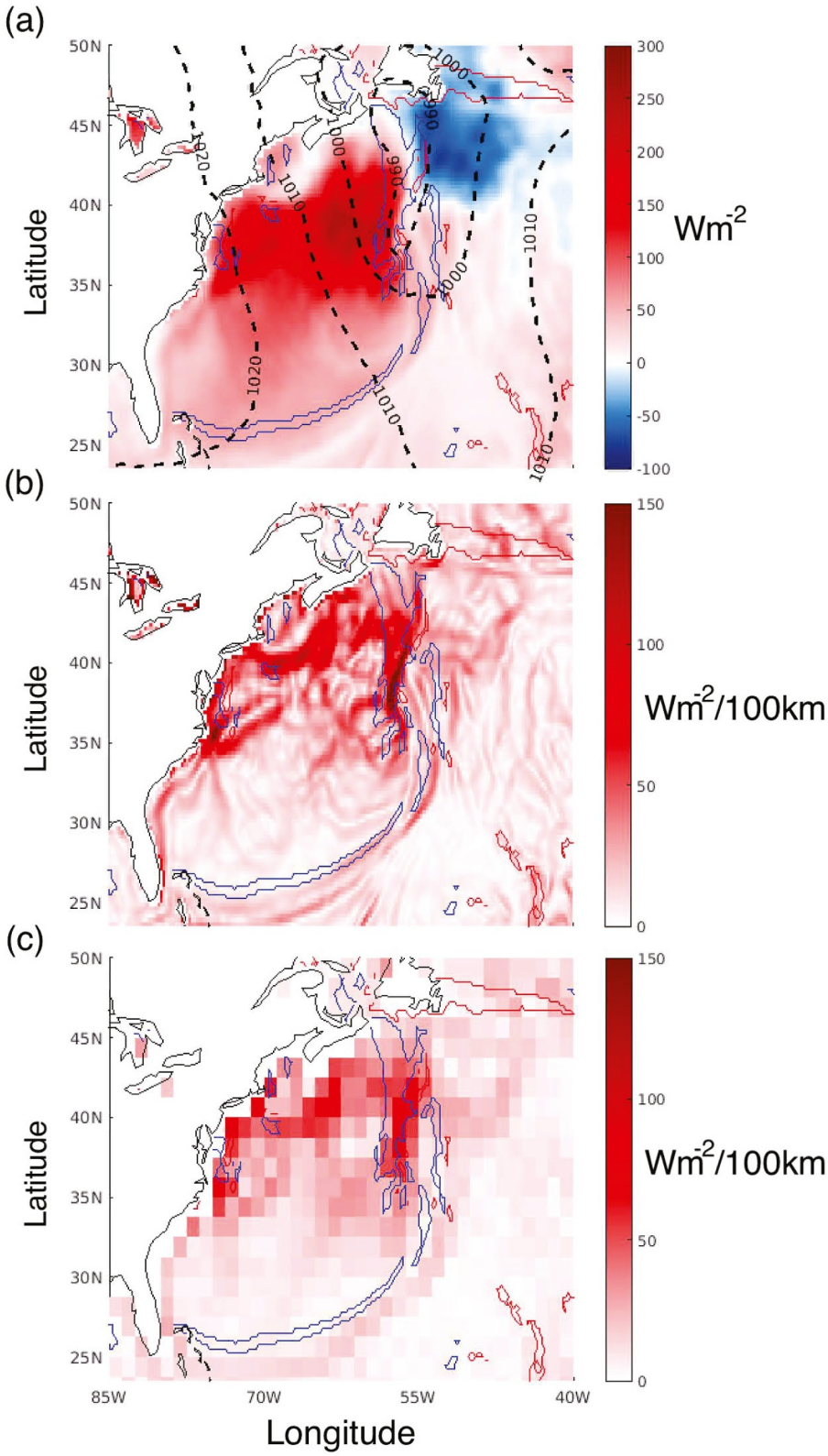

Figure 2. An extra-tropical cyclone in the North Atlantic identified in ERA-5 at 1200UTC 20 January 1979. (a) SHF (color, positive defined as ocean to atmosphere), mean sea-level pressure (dotted black contours), and atmospheric cold and warm fronts (blue and red contours). (b) $|\nabla \mathrm{SHF}|_{\sim 50\mathrm{km}}$, with atmospheric fronts overlaid. (c) $|\nabla \mathrm{SHF}|_{\sim 250\mathrm{km}}$, with atmospheric fronts overlaid.

(warm) fronts at 900 hPa in blue (red) contours. As expected, a broad region of strong ocean-to-atmosphere (atmosphere-to-ocean) SHF exists in the cold (warm) sector, associated with the air mass influence on $\Delta\theta$. At first glance, the SHFs in each sector appear relatively homogeneous. However, analysis of $|\nabla \mathrm{SHF}|_{\sim 50\mathrm{km}}$ in Figure 2b illustrates fine-scale underlying structure, with the strongest $|\nabla \mathrm{SHF}|_{\sim 50\mathrm{km}}$ located both in the cold sector and across the cold-front north of ∼37.5 N, likely associated with co-located sharp SST and atmospheric temperature gradients. It is noted that larger $|\nabla \mathrm{SHF}|_{\sim 50\mathrm{km}}$ are not always exactly co-located with the 900 hPa cold front due to cold frontal tilt with height. Such $|\nabla \mathrm{SHF}|_{\sim 50\mathrm{km}}$ are expected to strongly modulate the atmospheric temperature gradients within the storm.

Figure 2c illustrates the same as Figure 2b, however for a different gradient spatial scale, $|\nabla \mathrm{SHF}|_{\sim 250\mathrm{km}}$—that is, the SHF gradient magnitude is calculated using neighboring grid points 1.25° away, instead of 0.25°. The resulting magnitudes are much smaller everywhere; in weather or climate modeling experiments at these resolutions, there will therefore be noticeable impacts on the associated air-sea interaction processes. Additionally, while the spatial structure is naturally much coarser, there are areas (e.g., just after GS separation at ∼35 N) where the structure is significantly different. The disparity between the two spatial scales can also be seen for $\frac{d\mathrm{SHF}}{dy}$ and $\frac{d\mathrm{SHF}}{dx}$ (Figure S2 in Supporting Information S1). Indeed, many modeling studies in past decades have considered the impact of smoothed/coarser WBC SST gradients on mid-latitude storm-tracks, yet have often arrived at differing conclusions (e.g., Booth et al., 2012; Brayshaw et al., 2011; De Vries et al., 2019; Woollings et al., 2010). Indeed, the question regarding the extent to which SST gradients impact the mid-latitude atmosphere is still relatively open (Seo et al., 2023). Much of this disagreement may result from a lack of consistency in the smoothing methodology, either in region considered, method employed, or SST data set used, and indirectly the spatial scales at which the SST gradient is smoothed.

3.3. Product Comparison

To further discussion on the importance of specificity when calculating SHF and LHF gradients, distributions on various scales and in various different products are considered at (70 W, 37.5 N) in the GS for a common period DJF 1985–2018. Three products are considered, OAFlux-v3 (1°, daily means), JRA-55 (1.25°, 6-hourly) and ERA-5 (0.25°, hourly sampled every 6-hr).

Firstly, SHF and LHF in OAFlux-v3 and ERA-5 are interpolated to the JRA-55 grid. Then, daily averages are calculated in JRA-55 and ERA-5 from values at 6-hourly intervals (0000, 0600, 1200, 1800 UTC, calculated as described in Section 2). $\left(\frac{d\mathrm{SHF}}{dy}\right)_{\sim 250\mathrm{km,daily}}$ and $\left(\frac{d\mathrm{LHF}}{dy}\right)_{\sim 250\mathrm{km,daily}}$ are then calculated every day at (70 W, 37.5 N) from these daily means, and the probability distributions are plotted in Figures 3a and 3d respectively. For $\left(\frac{d\mathrm{SHF}}{dy}\right)_{\sim 250\mathrm{km,daily}}$, mean values for all three products are relatively close to zero, although there is significant variability across both positive and negative values (maximum and minimum values are also provided for reference). For values close to zero, JRA-55 and OAFlux-v3 are in good agreement, however notable divergence begins to occur as the absolute magnitudes increase. The distribution of values in ERA-5 are weighted much more heavily to larger positive magnitudes. For $\left(\frac{d\mathrm{LHF}}{dy}\right)_{\sim 250\mathrm{km,daily}}$, despite the mean values in each product being in good agreement, the distributions in all products exhibit much more disagreement than for $\left(\frac{d\mathrm{SHF}}{dy}\right)_{\sim 250\mathrm{km,daily}}$ across all values. Again, the distribution of values in ERA-5 are weighted the most heavily to larger absolute magnitudes.

Next, SHF and LHF values in JRA-55 and ERA-5 are used at 6-hourly intervals to calculate distributions of $\left(\frac{d\mathrm{SHF}}{dy}\right)_{\sim 250\mathrm{km}}$ and $\left(\frac{d\mathrm{LHF}}{dy}\right)_{\sim 250\mathrm{km}}$ at the same location (Figures 3b and 3e respectively). As expected, by removing daily temporal averaging, the mean values stay the same but distribution spread increases. In particular, absolute magnitudes of $\left(\frac{d\mathrm{SHF}}{dy}\right)_{\sim 250\mathrm{km}}$ above $50\mathrm{Wm}^{-2}/100$ km and $\left(\frac{d\mathrm{LHF}}{dy}\right)_{\sim 250\mathrm{km}}$ above $100\mathrm{Wm}^{-2}/100$ km are observed more frequently than in the daily means, suggesting $\left(\frac{d\mathrm{SHF}}{dy}\right)_{\sim 250\mathrm{km}}$ and $\left(\frac{d\mathrm{LHF}}{dy}\right)_{\sim 250km}$ of these magnitudes typically persist here less than a day. Similar to the daily means, $\left(\frac{d\mathrm{SHF}}{dy}\right)_{\sim 250\mathrm{km}}$ and $\left(\frac{d\mathrm{LHF}}{dy}\right)_{\sim 250\mathrm{km}}$ distributions in ERA-5 generally exhibit fatter tails than those in JRA-55.

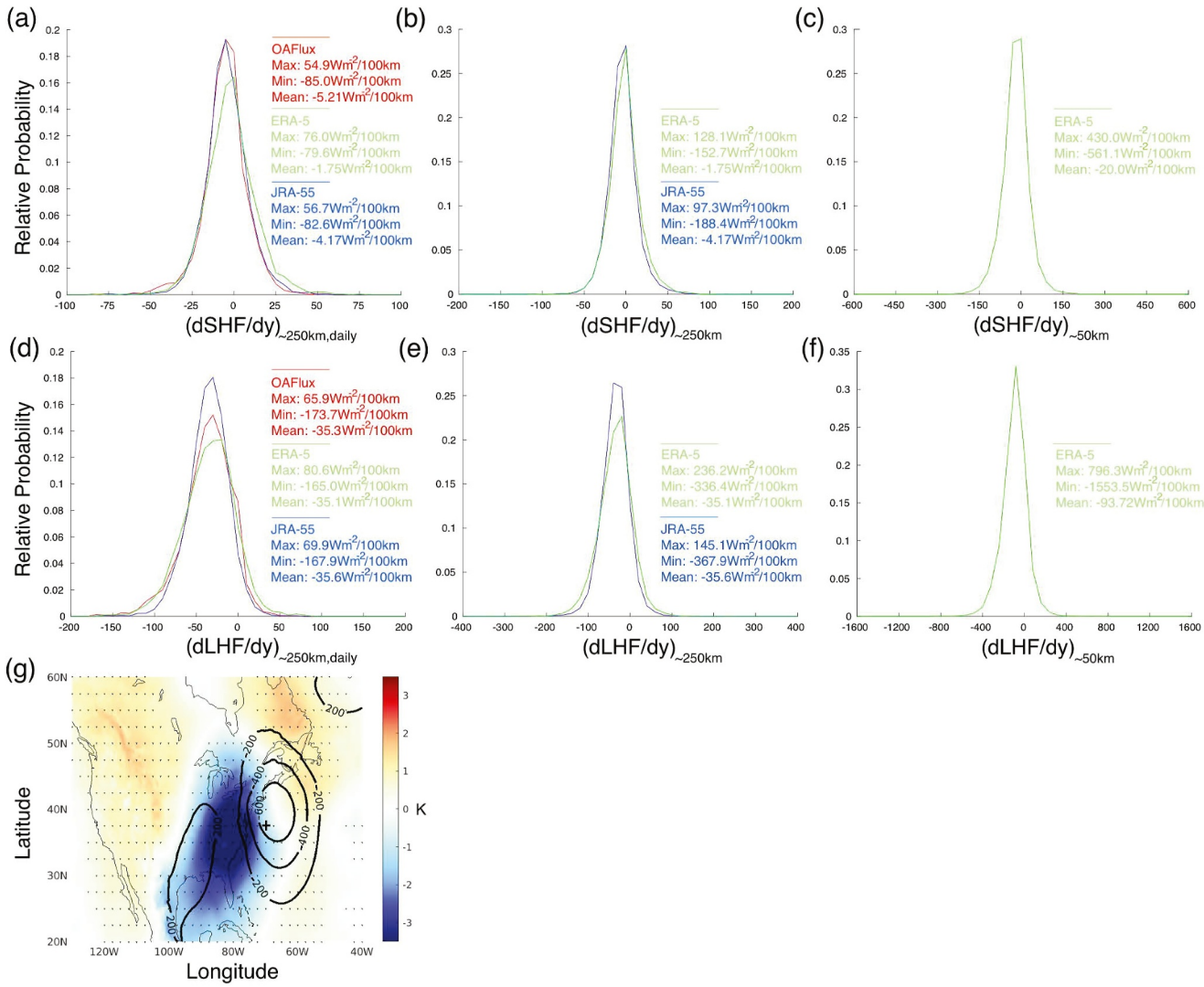

Figure 3. (a) Distribution of $\left(\frac{dSHF}{dy}\right)_{\sim 250km,daily}$ at 70 W, 37.5 N (Wm^{-2}/100 km) for DJF 1985–2018 in OAFlux-v3, JRA-55 and ERA-5. (b) As in panel (a), but for $\left(\frac{dSHF}{dy}\right)_{\sim 250km}$ in JRA-55 (6-hourly) and ERA-5 (hourly, sampled 6-hourly). (c) As in panel (a), but for $\left(\frac{dSHF}{dy}\right)_{\sim 50km}$ in ERA-5 (hourly, sampled 6-hourly). (d)–(f) As in panels (a–c) respectively, but for $\frac{dLHF}{dy}$. (g) 900 hPa temperature anomalies in color (dotted statistical significance to 95%), with contoured mean sea-level pressure anomalies, composited on times when $\left(\frac{dSHF}{dy}\right)_{\sim 50km} < -100$ Wm^{-2}/100 km at 70 W, 37.5 N (marked with a cross).

Lastly, SHF and LHF values in ERA-5 are used at 6-hourly intervals, on their original 0.25° grid to calculate distributions of $\left(\frac{dSHF}{dy}\right)_{\sim 50km}$ and $\left(\frac{dLHF}{dy}\right)_{\sim 50km}$ at the same location (Figures 3c and 3f respectively), with the units still in Wm^{-2}/100 km. At these spatial scales, the absolute magnitude of the mean increases noticeably. Furthermore, values over three to four times larger are found in $\left(\frac{dSHF}{dy}\right)_{\sim 50km}$ and $\left(\frac{dLHF}{dy}\right)_{\sim 50km}$ than in $\left(\frac{dSHF}{dy}\right)_{\sim 250km}$ and $\left(\frac{dLHF}{dy}\right)_{\sim 250km}$, indicative of significant finer-scale variability at this location that would not be captured in a data set of lower spatial resolution. Figure 3g illustrates atmospheric 900 hPa temperature anomalies in color (dotted statistical significance to 95%), with contoured MSLP anomalies, composited on times when $\left(\frac{dSHF}{dy}\right)_{\sim 50km} < -100$ Wm^{-2}/100 km at (70 W, 37.5 N). These $\left(\frac{dSHF}{dy}\right)_{\sim 50km}$ magnitudes not found at ~250 km scales are typically associated with sharp atmospheric temperature gradients embedded within extra-tropical cyclones, that is, atmospheric fronts.

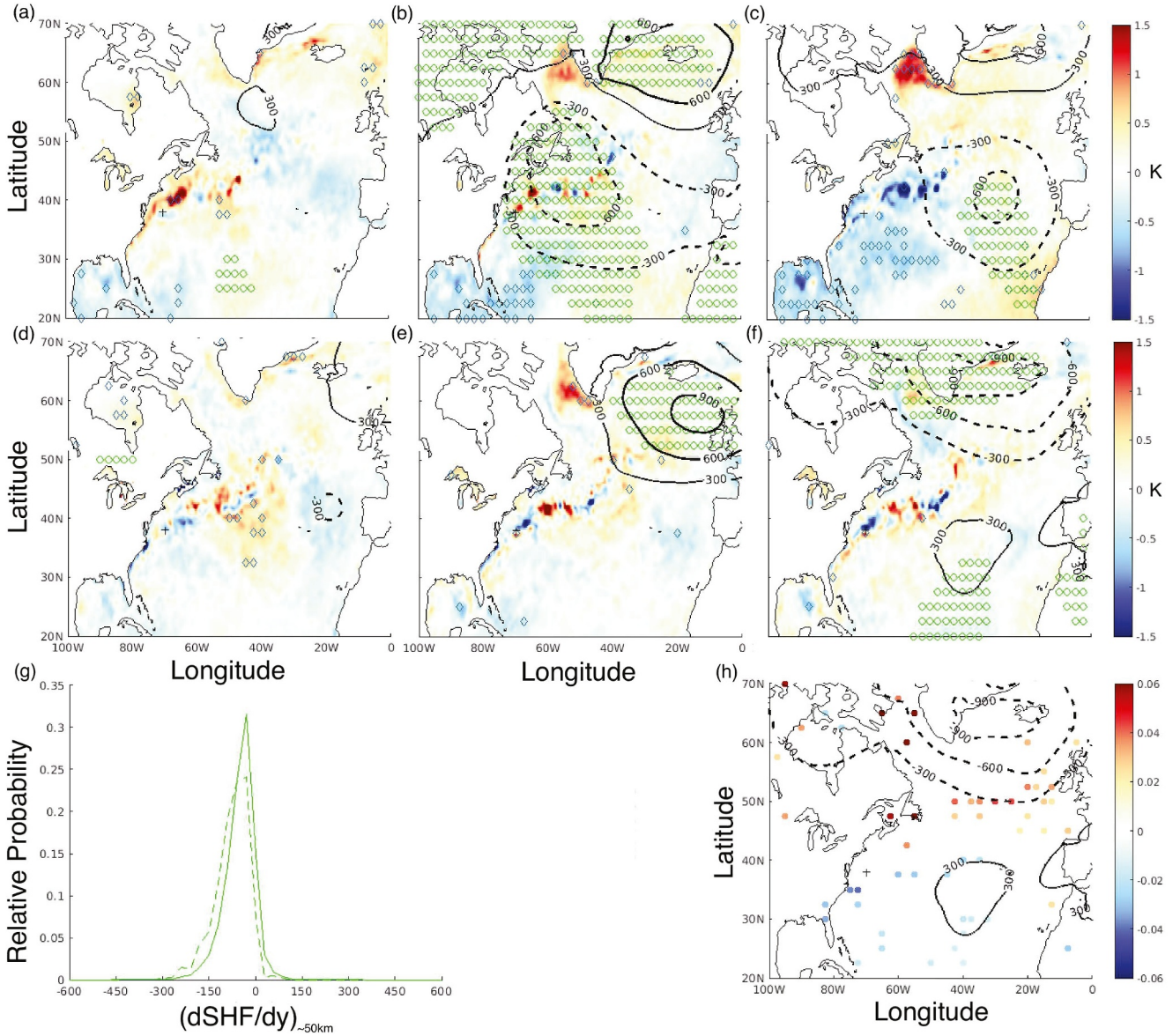

Figure 4. Monthly (a) December (−1 month) (b) January (simultaneous) (c) February (+1 month) anomalies in sea-surface temperature (SST) (color) and mean sea-level pressure (MSLP) (contours), composited on the 10% most positive January monthly mean values of SHF at 70 W, 38 N during the period DJF 1979–2018. Statistical significance to 90% shown for SST (blue diamonds) and MSLP (green circles). (d–f) As in panels (a–c) except composited on the 10% most negative January monthly mean values of $\left(\frac{dSHF}{dy}\right)_{\sim 50km}$. (g) Distribution of $\left(\frac{dSHF}{dy}\right)_{\sim 50km}$ at 70 W, 38 N (Wm^{-2}/100 km) for the DJF seasons used in the panels (d–f) composites (dotted green), as well as for DJF 1979–2018 (solid green). (h) As in panels (f) but with atmospheric cold frontal anomalies, where significant to 95%, plotted as colored circles.

3.4. Influence of Air-Sea Flux Gradients on the North Atlantic Oscillation

Traditionally, extra-tropical air-sea heat fluxes are viewed as being driven mainly by atmospheric variability. For example, the leading monthly mode of North Atlantic SST variability has been extensively noted to reflect variability in the North Atlantic Oscillation (NAO) and subsequent atmospheric forcing of the air-sea heat fluxes (c.f. Figure 2, Marshall et al., 2001). Figure 4 shows the ERA-5 lead-lag composite [(a) −1 month, December, (b) 0 lag, January, and (c) +1 month, February] of both monthly SST (color) and MSLP (contours) anomalies, composited on the 10% most positive (i.e., ocean-to-atmosphere) monthly January-mean SHF values at 70 W, 38 N between 1979 and 2018. Significance as measured by a two-sample *t*-test to 90% is shown as blue diamonds (green circles) for SST (MSLP). Strong monthly January SHF is associated with strong co-located anomalous low-pressure (Parfitt & Czaja, 2016; Zolina & Gulev, 2003), appearing as part of the basin-wide NAO-negative

signal. In February, the basin-wide MSLP signal dissipates and significant SST anomalies become more widespread. Although the composite sample size is small, the NAO-SHF relationship can also be seen in a 39-season correlation of anomalous monthly January SHF at this location with the monthly NAO index (Hurrell et al., 2003) in January ($r = -0.40$, $p = 0.01$) and February (negligible).

The same procedure as in Figures 4a–4c is now applied to the most negative 10% of monthly mean January $\left(\frac{d\mathrm{SHF}}{dy}\right)_{\sim 50\mathrm{km}}$ values in Figures 4d–4f. There is little basin-wide signal in either SST or MSLP at zero lag (although anomalous high-pressure exists to the east of Greenland, and a statistically significant SST anomaly at the location itself). Instead, a basin-wide NAO-type MSLP (but not SST) anomaly is found in February. Indeed, the analogous 39-season correlation between anomalous monthly January $\left(\frac{d\mathrm{SHF}}{dy}\right)_{\sim 50\mathrm{km}}$ at this location and the monthly January NAO index is negligible, but weakly significant 1 month later for the February NAO ($r = -0.28$, $p = 0.08$). Neighboring grid-points more strongly exhibit this relationship between anomalous monthly January $\left(\frac{d\mathrm{SHF}}{dy}\right)_{\sim 50\mathrm{km}}$ and the February NAO index (e.g., 70 W, 38.25 N: $r = -0.33$, $p = 0.04$; 70 W, 38.5 N: $r = -0.31$, $p = 0.05$). However, the grid-point used in Figure 3 does not (70 W, 37.5 N), nor does point (70 W, 38.75 N); these points have an average $\left(\frac{d\mathrm{SHF}}{dy}\right)_{\sim 50\mathrm{km}}$ considerably closer to zero than the points exhibiting the relationship, likely due to increased distance from the average GS frontal axis. It is worth noting that a data set with values every 1.25° would not pick up the three points of significance discussed above.

The intention here is simply to illustrate how air-sea flux gradients provide information separate from air-sea fluxes alone, with detailed dynamical exploration left for a companion study. However, Parfitt and Kwon (2020) discussed how an enhanced $\left(\frac{d\mathrm{SHF}}{dy}\right)_{\sim 50\mathrm{km}}$ (note this equates to more negative values at this location) can impact diabatic frontogenesis and potentially the eddy-driven jet latitude, offering one potential explanation for the relationship in Figure 4f. Figure 4g shows the DJF distribution of $\left(\frac{d\mathrm{SHF}}{dy}\right)_{\sim 50\mathrm{km}}$ for the four seasons used in Figure 4f and demonstrates that significant negative $\left(\frac{d\mathrm{SHF}}{dy}\right)_{\sim 50\mathrm{km}}$ are much more common than in typical DJF seasons. Figure 4h illustrates the same as Figure 4f, except instead of SST, monthly atmospheric cold frontal anomalies are plotted as dots where they are significant to 95%. The units are of absolute fractional frequency (i.e., 0.06 would mean a cold front is identified here, say, 14% of the time in February vs. a February average of 8%). Comparison with typical atmospheric frontal climatologies (e.g., Berry et al., 2011; Soster & Parfitt, 2022) show these anomalies reach percentage changes of ∼50%, and are consistent with the MSLP anomalies (i.e., more atmospheric cold fronts with lower MSLP and vice versa).

4. Discussion

Despite several studies illustrating the importance of SHF and LHF gradients, the statistics of their variability, their representation in data products, and their overall influence on weather and climate are rarely discussed in the literature. This study presents a wintertime climatology of meridional SHF and LHF gradients at the ∼50 km scale in ERA-5. Generally, large climatological magnitudes are found at oceanic frontal zones, regions with large SST gradients. This is unsurprising, given that mesoscale SHF and LHF fluxes have recently been argued as ocean-driven. In reanalyses and models this is significant (e.g., Kirtman et al., 2012), and only recently have we been able to represent such fine-scale heat fluxes—for example, the average SST resolution in the Coupled Model Intercomparison Project 5 (Taylor et al., 2012) was only ∼1°.

Often, air-sea interaction studies considering gradients do not specify the scales that are being considered, potentially leading to inconsistency between conclusions (a well-known instance is the importance of the GS SST gradient for North Atlantic variability). A case study of $|\nabla \mathrm{SHF}|_{\sim 50\mathrm{km}}$ and $|\nabla \mathrm{SHF}|_{\sim 250\mathrm{km}}$ within an extra-tropical cyclone demonstrates clear differences - a model experiment at these different resolutions, or with SST smoothing at these different scales, will impact the atmospheric system differently. Studies have also shown explicitly that GS gradient variability at ∼50km is different from that at larger scales (Parfitt et al., 2022), and modeling studies to further ascertain the sensitivity of ocean-weather interactions to different scales in $|\nabla \mathrm{SHF}|$ and $|\nabla \mathrm{LHF}|$ would be useful.

Significant differences between three different data products are illustrated across the GS in distributions of $\left(\frac{d\mathrm{SHF}}{dy}\right)_{\sim 250\mathrm{km,daily}}$, $\left(\frac{d\mathrm{SHF}}{dy}\right)_{\sim 250\mathrm{km}}$ and $\left(\frac{d\mathrm{SHF}}{dy}\right)_{\sim 50\mathrm{km}}$. A notable issue is that there are almost no corresponding in situ observations to validate these products in such regions (e.g., buoys that remain a constant distance close to each other). The fact that large disagreements primarily exist in the distribution tails, often induced by fast-moving atmospheric fronts, also means that satellite-derived flux products cannot serve as a validation tool either. This is because input variables come from different satellites with different overpass times (Gentemann et al., 2020); for example, the product Institut Français pour la Recherche et l'Exploitation de la Mer (Bentamy et al., 2013) bins observations in a 3-hr window, whereas the Japanese Ocean Flux Data Sets with Use of Remote Sensing Observations product (Tomita et al., 2019) bins over an entire day.

Lastly, an example is shown of monthly variability in GS $\left(\frac{d\mathrm{SHF}}{dy}\right)_{\sim 50\mathrm{km}}$ statistically preceding the NAO by a month, but with high sensitivity to the exact location (to < 100km). Such results provide clear evidence of the need to expand in situ networks (e.g., Clayson et al., 2021; Diard et al., 2019), especially away from coastlines, and improve satellite-derived products. Future open ocean observational deployments should include methodologies (e.g., multiple in situ platforms, Farrar et al., 2020; in-tandem uncrewed surface vehicles, Cronin et al., 2024) for maintaining air-sea flux measurements at consistent distances (in particular < 250km) from each other for extended periods.

Data Availability Statement

ERA5 (Hersbach et al., 2023) data can be freely obtained from the Climate Data Store. JRA-55 (Japan Meteorological Agency, 2013) data can be freely obtained from the Research Data Archive, as can OAFlux v3 (Goddard Institute for Space Studies et al., 2006). The NAO index (Hurrell et al., 2023) is available from the Climate Data Guide.

Acknowledgments
The author thanks ECMWF for access to ERA5, the Japan Meteorological Agency for access to JRA-55, NASA and Woods Hole Oceanographic Institution for access to OAFlux-v3, the National Center for Atmospheric Research for access to the NAO index, and Frederick Soster for assistance with the frontal data. Support from NSF OCE-2023585, NSF OCE-2123632, and NOAA CVP NA22OAR4310617 is acknowledged. The comments of two anonymous reviewers are greatly appreciated.

References

Bentamy, A., Grodsky, S. A., Katsaros, K., Mestas-Nuñez, A. M., Blanke, B., & Desbiolles, F. (2013). Improvement in air–sea flux estimates derived from satellite observations. *International Journal of Remote Sensing*, *34*(14), 5243–5261. https://doi.org/10.1080/01431161.2013.787502

Berry, G., Reeder, M. J., & Jakob, C. (2011). A global climatology of atmospheric fronts. *Geophysical Research Letters*, *38*(4), L04809. https://doi.org/10.1029/2010gl046451

Bishop, S. P., Small, R. J., Bryan, F. O., & Tomas, R. A. (2017). Scale dependence of midlatitude air–sea interaction. *Journal of Climate*, *30*(20), 8207–8221. https://doi.org/10.1175/jcli-d-17-0159.1

Booth, J. F., Thompson, L., Patoux, J., & Kelly, K. A. (2012). Sensitivity of midlatitude storm intensification to perturbations in the sea surface temperature near the Gulf Stream. *Monthly Weather Review*, *140*(4), 1241–1256. https://doi.org/10.1175/mwr-d-11-00195.1

Brayshaw, D. J., Hoskins, B., & Blackburn, M. (2011). The basic ingredients of the North Atlantic storm track. Part II: Sea surface temperatures. *Journal of the Atmospheric Sciences*, *68*(8), 1784–1805. https://doi.org/10.1175/2011jas3674.1

Cione, J. J., Raman, S., & Pietrafesa, L. J. (1993). The effect of Gulf Stream-induced baroclinicity on US East Coast winter cyclones. *Monthly Weather Review*, *121*(2), 421–430. https://doi.org/10.1175/1520-0493(1993)121<0421:teogsi>2.0.co;2

Clayson, C. A., Centurioni, L., Cronin, M. F., Edson, J., Gille, S., Muller-Karger, F., et al. (2021). Super sites for advancing understanding of the oceanic and atmospheric boundary layers. *Marine Technology Society Journal*, *55*(3), 144–145. https://doi.org/10.4031/mtsj.55.3.11

Cronin, M. F., Gentemann, C. L., Edson, J., Ueki, I., Bourassa, M., Brown, S., et al. (2019). Air-sea fluxes with a focus on heat and momentum. *Frontiers in Marine Science*, *6*, 430. https://doi.org/10.3389/fmars.2019.00430

Cronin, M. F., Zhang, D., Wills, S. M., Reeves Eyre, J. J., Thompson, L., & Anderson, N. (2024). Diurnal warming rectification in the tropical Pacific linked to sea surface temperature front. *Nature Geoscience*, *17*(4), 316–322. https://doi.org/10.1038/s41561-024-01391-8

Diard, M. B., Bishop, S. P., & Donohue, K. A. (2019). Wintertime surface heat and momentum fluxes in the Gulf Stream from saildrone observations. *SURFO Technical Report No. 19-02*, *1*.

Farrar, J. T., D'Asaro, E., Rodriguez, E., Shcherbina, A., Czech, E., Matthias, P., et al. (2020). S-MODE: The sub-mesoscale ocean dynamics experiment. In *IGARSS 2020-2020 IEEE international geoscience and remote sensing symposium* (pp. 3533–3536). IEEE.

Gentemann, C. L., Clayson, C. A., Brown, S., Lee, T., Parfitt, R., Farrar, J. T., et al. (2020). Fluxsat: Measuring the ocean–atmosphere turbulent exchange of heat and moisture from space. *Remote Sensing*, *12*(11), 1796. https://doi.org/10.3390/rs12111796

Goddard Institute for Space Studies, Earth Sciences Division, Science and Exploration Directorate, Goddard Space Flight Center, NASA, and Physical Oceanography Department, & Woods Hole Oceanographic Institution (2006). Objectively Analyzed Air-Sea Fluxes (OAFlux) For Global Oceans, By Lisan Yu et al. [Dataset]. *Research Data Archive at the National Center for Atmospheric Research, Computational and Information Systems Laboratory*. https://doi.org/10.5065/0JDQ-FP94

Hersbach, H., Bell, B., Berrisford, P., Biavati, G., Horányi, A., Muñoz Sabater, J., et al. (2023). ERA5 hourly data on single levels from 1940 to present [Dataset]. *Copernicus Climate Change Service (C3S) Climate Data Store (CDS)*. https://doi.org/10.24381/cds.adbb2d47

Hersbach, H., Bell, B., Berrisford, P., Hirahara, S., Horányi, A., Muñoz-Sabater, J., et al. (2020). The ERA5 global reanalysis. *Quarterly Journal of the Royal Meteorological Society*, *146*(730), 1999–2049. https://doi.org/10.1002/qj.3803

Hirata, H., Kawamura, R., Nonaka, M., & Tsuboki, K. (2019). Significant impact of heat supply from the Gulf Stream on a "superbomb" cyclone in January 2018. *Geophysical Research Letters*, *46*(13), 7718–7725. https://doi.org/10.1029/2019gl082995

Hotta, D., & Nakamura, H. (2011). On the significance of the sensible heat supply from the ocean in the maintenance of the mean baroclinicity along storm tracks. *Journal of Climate*, *24*(13), 3377–3401. https://doi.org/10.1175/2010jcli3910.1

Hurrell, J., & Phillips, A., & National Center for Atmospheric Research Staff. (2023). [Dataset]. In *Last modified 2023-07-10: "The climate data Guide: Hurrell North Atlantic Oscillation (NAO) index (station-based)*. Retrieved from https://climatedataguide.ucar.edu/climate-data/hurrell-north-atlantic-oscillation-nao-index-station-based

Hurrell, J. W., Kushnir, Y., Ottersen, G., & Visbeck, M. (2003). An overview of the North Atlantic oscillation. *Geophysical Monograph-American Geophysical Union*, *134*, 1–36.

Jacobs, N. A., Raman, S., Lackmann, G. M., & Childs Jr, P. P. (2008). The influence of the Gulf Stream induced SST gradients on the US East Coast winter storm of 24–25 January 2000. *International Journal of Remote Sensing*, *29*(21), 6145–6174. https://doi.org/10.1080/01431160802175561

Japan Meteorological Agency, J. (2013). Updated monthly. JRA-55: Japanese 55-year reanalysis, daily 3-hourly and 6-hourly data [Dataset]. *Research Data Archive at the National Center for Atmospheric Research, Computational and Information Systems Laboratory*. https://doi.org/10.5065/D6HH6H41

Jin, X., & Weller, R. A. (2008). Multidecade global flux datasets from the objectively analyzed Air-sea Fluxes (OAFlux) Project: Latent and sensible heat fluxes, ocean evaporation, and related surface meteorological variables. In *OAFlux*. Woods Hole Oceanographic Institution.

Jones, E., Parfitt, R., & Wing, A. A. (2024). Development of frontal boundaries during the extratropical transition of tropical cyclones. *Quarterly Journal of the Royal Meteorological Society*, *150*(759), 995–1011. https://doi.org/10.1002/qj.4633

Jones, E., Parfitt, R., Wing, A. A., & Hart, R. (2023). Gulf Stream sea surface temperature anomalies associated with the extratropical transition of North Atlantic tropical cyclones. *Geophysical Research Letters*, *50*(16), e2023GL102904. https://doi.org/10.1029/2023gl102904

Joyce, T. M., Kwon, Y. O., Seo, H., & Ummenhofer, C. C. (2019). Meridional Gulf Stream shifts can influence wintertime variability in the North Atlantic storm track and Greenland blocking. *Geophysical Research Letters*, *46*(3), 1702–1708. https://doi.org/10.1029/2018gl081087

Kawai, Y., Miyama, T., Iizuka, S., Manda, A., Yoshioka, M. K., Katagiri, S., et al. (2015). Marine atmospheric boundary layer and low-level cloud responses to the Kuroshio extension front in the early summer of 2012: Three-vessel simultaneous observations and numerical simulations. *Journal of Oceanography*, *71*(5), 511–526. https://doi.org/10.1007/s10872-014-0266-0

Kirtman, B. P., Bitz, C., Bryan, F., Collins, W., Dennis, J., Hearn, N., et al. (2012). Impact of ocean model resolution on CCSM climate simulations. *Climate Dynamics*, *39*(6), 1303–1328. https://doi.org/10.1007/s00382-012-1500-3

Kobayashi, S., Ota, Y., Harada, Y., Ebita, A., Moriya, M., Onoda, H., et al. (2015). The JRA-55 reanalysis: General specifications and basic characteristics. *Journal of the Meteorological Society of Japan. Ser. II*, *93*(1), 5–48. https://doi.org/10.2151/jmsj.2015-001

Marshall, J., Kushnir, Y., Battisti, D., Chang, P., Czaja, A., Dickson, R., et al. (2001). North Atlantic climate variability: Phenomena, impacts and mechanisms. *International Journal of Climatology: A Journal of the Royal Meteorological Society*, *21*(15), 1863–1898. https://doi.org/10.1002/joc.693

Masunaga, R., Nakamura, H., Kamahori, H., Onogi, K., & Okajima, S. (2018). JRA-55CHS: An atmospheric reanalysis produced with high-resolution SST. *Sola*, *14*(0), 6–13. https://doi.org/10.2151/sola.2018-002

Minobe, S., Kuwano-Yoshida, A., Komori, N., Xie, S. P., & Small, R. J. (2008). Influence of the Gulf Stream on the troposphere. *Nature*, *452*(7184), 206–209. https://doi.org/10.1038/nature06690

Nakamura, H., Sampe, T., Tanimoto, Y., & Shimpo, A. (2004). Observed associations among storm tracks, jet streams and midlatitude oceanic fronts. *Earth's Climate: The Ocean–Atmosphere Interaction, Geophys. Monogr*, *147*, 329–345. https://doi.org/10.1029/147gm18

Parfitt, R., & Czaja, A. (2016). On the contribution of synoptic transients to the mean atmospheric state in the Gulf Stream region. *Quarterly Journal of the Royal Meteorological Society*, *142*(696), 1554–1561. https://doi.org/10.1002/qj.2689

Parfitt, R., Czaja, A., & Kwon, Y. O. (2017). The impact of SST resolution change in the ERA-Interim reanalysis on wintertime Gulf Stream frontal air-sea interaction. *Geophysical Research Letters*, *44*(7), 3246–3254. https://doi.org/10.1002/2017gl073028

Parfitt, R., Czaja, A., Minobe, S., & Kuwano-Yoshida, A. (2016). The atmospheric frontal response to SST perturbations in the Gulf Stream region. *Geophysical Research Letters*, *43*(5), 2299–2306. https://doi.org/10.1002/2016gl067723

Parfitt, R., Czaja, A., & Seo, H. (2017b). A simple diagnostic for the detection of atmospheric fronts. *Geophysical Research Letters*, *44*(9), 4351–4358. https://doi.org/10.1002/2017gl073662

Parfitt, R., Kwon, Y., & Andres, M. (2022). A monthly index for the large-scale sea surface temperature gradient across the separated Gulf Stream. *Geophysical Research Letters*, *49*(24), e2022GL100914. https://doi.org/10.1029/2022gl100914

Parfitt, R., & Kwon, Y. O. (2020). The modulation of Gulf Stream influence on the troposphere by the eddy-driven jet. *Journal of Climate*, *33*(10), 4109–4120. https://doi.org/10.1175/jcli-d-19-0294.1

Parfitt, R., & Seo, H. (2018). A new framework for near-surface wind convergence over the Kuroshio extension and Gulf Stream in wintertime: The role of atmospheric fronts. *Geophysical Research Letters*, *45*(18), 9909–9918. https://doi.org/10.1029/2018gl080135

Reeder, M. J., Spengler, T., & Spensberger, C. (2021). The effect of sea surface temperature fronts on atmospheric frontogenesis. *Journal of the Atmospheric Sciences*, *78*(6), 1753–1771. https://doi.org/10.1175/jas-d-20-0118.1

Robertson, F. R., Roberts, J. B., Bosilovich, M. G., Bentamy, A., Clayson, C. A., Fennig, K., et al. (2020). Uncertainties in ocean latent heat flux variations over recent decades in satellite-based estimates and reduced observation reanalyses. *Journal of Climate*, *33*(19), 8415–8437. https://doi.org/10.1175/jcli-d-19-0954.1

Sampe, T., Nakamura, H., Goto, A., & Ohfuchi, W. (2010). Significance of a midlatitude SST frontal zone in the formation of a storm track and an eddy-driven westerly jet. *Journal of Climate*, *23*(7), 1793–1814. https://doi.org/10.1175/2009jcli3163.1

Seo, H., O'Neill, L. W., Bourassa, M. A., Czaja, A., Drushka, K., Edson, J. B., et al. (2023). Ocean mesoscale and frontal-scale ocean–atmosphere interactions and influence on large-scale climate: A review. *Journal of Climate*, *36*(7), 1981–2013. https://doi.org/10.1175/jcli-d-21-0982.1

Small, R. J., Bryan, F. O., Bishop, S. P., & Tomas, R. A. (2019). Air–sea turbulent heat fluxes in climate models and observational analyses: What drives their variability? *Journal of Climate*, *32*(8), 2397–2421. https://doi.org/10.1175/jcli-d-18-0576.1

Soster, F., & Parfitt, R. (2022). On objective identification of atmospheric fronts and frontal precipitation in reanalysis datasets. *Journal of Climate*, *35*(14), 4513–4534. https://doi.org/10.1175/jcli-d-21-0596.1

Taguchi, B., Nakamura, H., Nonaka, M., & Xie, S. P. (2009). Influences of the Kuroshio/Oyashio Extensions on air–sea heat exchanges and storm-track activity as revealed in regional atmospheric model simulations for the 2003/04 cold season. *Journal of Climate*, *22*(24), 6536–6560. https://doi.org/10.1175/2009jcli2910.1

Taylor, K. E., Stouffer, R. J., & Meehl, G. A. (2012). An Overview of CMIP5 and the experiment design. *Bulletin America Meteorology Social*, *93*(4), 485–498. https://doi.org/10.1175/BAMS-D-11-00094.1

Tochimoto, E., & Niino, H. (2022). Comparing frontal structures of extratropical cyclones in the northwestern Pacific and northwestern Atlantic storm tracks. *Monthly Weather Review*, *150*(2), 369–392. https://doi.org/10.1175/mwr-d-21-0181.1

Tomita, H., Hihara, T., Kako, S. I., Kubota, M., & Kutsuwada, K. (2019). An introduction to J-OFURO3, a third-generation Japanese ocean flux data set using remote-sensing observations. *Journal of Oceanography*, *75*(2), 171–194. https://doi.org/10.1007/s10872-018-0493-x

Tozuka, T., & Cronin, M. F. (2014). Role of mixed layer depth in surface frontogenesis: The Agulhas Return Current front. *Geophysical Research Letters*, *41*(7), 2447–2453. https://doi.org/10.1002/2014gl059624

Tozuka, T., Cronin, M. F., & Tomita, H. (2017). Surface frontogenesis by surface heat fluxes in the upstream Kuroshio Extension region. *Scientific Reports*, *7*(1), 10258. https://doi.org/10.1038/s41598-017-10268-3

Trenberth, K. E., & Caron, J. M. (2001). Estimates of meridional atmosphere and ocean heat transports. *Journal of Climate*, *14*(16), 3433–3443. https://doi.org/10.1175/1520-0442(2001)014<3433:eomaao>2.0.co;2

Vries, H. D., Scher, S., Haarsma, R., Drijfhout, S., & Delden, A. V. (2019). How Gulf-Stream SST-fronts influence Atlantic winter storms: Results from a downscaling experiment with HARMONIE to the role of modified latent heat fluxes and low-level baroclinicity. *Climate Dynamics*, *52*(9–10), 5899–5909. https://doi.org/10.1007/s00382-018-4486-7

Walland, D., & Simmonds, I. (1999). Baroclinicity, meridional temperature gradients, and the southern semiannual oscillation. *Journal of Climate*, *12*(12), 3376–3382. https://doi.org/10.1175/1520-0442(1999)012<3376:bmtgat>2.0.co;2

Woollings, T., Hoskins, B., Blackburn, M., Hassell, D., & Hodges, K. (2010). Storm track sensitivity to sea surface temperature resolution in a regional atmosphere model. *Climate Dynamics*, *35*(2–3), 341–353. https://doi.org/10.1007/s00382-009-0554-3

Yu, L., & Weller, R. A. (2007). Objectively analyzed air–sea heat fluxes for the global ice-free oceans (1981–2005). *Bulletin of the American Meteorological Society*, *88*(4), 527–540. https://doi.org/10.1175/bams-88-4-527

Zolina, O., & Gulev, S. K. (2003). Synoptic variability of ocean–atmosphere turbulent fluxes associated with atmospheric cyclones. *Journal of Climate*, *16*(16), 2717–2734. https://doi.org/10.1175/1520-0442(2003)016<2717:svootf>2.0.co;2